Synthesis of uniform $Fe_2O_3@Y_2O_3$ yolk−shell nanoreactors as chemical looping oxygen carriers

Qianwenhao Fan [a,b,1], Mingwu Tan [c,1], Bingqing Yao [d,1], Syed Saqline [a,b,e], Longgang Tao [c], Qian He [d], Wen Liu [a,b,e,*]

[a] School of Chemistry, Chemical Engineering and Biotechnology, Nanyang Technological University, 62 Nanyang Drive, Singapore 637459, Singapore
[b] Cambridge Centre for Advanced Research and Education in Singapore, 1 Create Way, Singapore 138602, Singapore
[c] Institute of Sustainability for Chemicals, Energy and Environment, Agency for Science, Technology and Research (A*STAR), 1 Pesek Road, Jurong Island, 627833, Singapore
[d] Department of Materials Science and Engineering, National University of Singapore, 9 Engineering, Drive 1, Singapore 117575, Singapore
[e] Nanyang Environmental and Water Research Institute, Nanyang Technological University, 1 Cleantech Loop, Singapore 637141, Singapore

ARTICLE INFO

ABSTRACT

Iron-based materials are extensively employed as oxygen carriers in chemical looping processes, but their long-term performance is often inhibited by sintering and agglomeration. Here, we developed a yolk–shell structured $Fe_2O_3@Y_2O_3$ oxygen carrier, with each unit consisting of a Y_2O_3 shell encapsulating a nano-sized Fe_2O_3 core. The Y_2O_3 shell could protect the redox-active cores from sintering, and the void between the yolk and the shell is capable of tolerating cyclic volume and phase changes. During the simulated chemical looping cycles at 600 °C, the $Fe_2O_3@Y_2O_3$ oxygen carriers exhibit a consistent oxygen carrying capacity of 3 wt% over 50 cycles, without any distinguishable structural deterioration. With rational structure optimization, the $Fe_2O_3@Y_2O_3$ oxygen carriers with porous shell could enhance the mass transfer across the shell and enable higher reaction rates. The satisfactory sintering resistance of the $Fe_2O_3@Y_2O_3$ nanostructure demonstrates the feasibility of employing well defined yolk–shell structured oxygen carriers for chemical looping applications.

1. Introduction

The world's energy demand is continuously growing, driven by industrialization, population growth, and the increasing need for electricity. This demand has traditionally been met by the combustion of fossil fuels, which has led to significant environmental drawbacks, including the emission of greenhouse gases such as CO_2 [1]. These emissions are a major contributor to global warming and climate change, prompting the need for new emission reduction technologies. One such promising technology is chemical looping, a class of process intensification technologies that break redox reactions into half redox reactions, mediated by redox-active solids, such as metal oxides. For instance the chemical looping combustion facilitates oxy-fuel combustion without an air separation unit, making it a potentially more efficient solution for carbon capture and storage [2]. In the redox reaction involves the transfer of oxygen, e.g., combustion [3,4], gasification [6,7],

air separation [8,9], reforming [10–12], oxidation dehydrogenation of alkanes [13–16], oxidative coupling [17–19], epoxidation [20–22], and thermochemical water splitting [23–25], the oxygen is transported between a reduction reactor and an oxidation reactor in the form of lattice oxygen, which is carried by oxygen carriers (typically a redox-active metal oxide), as illustrated in Fig. 1a [26]. In the fuel reactor, the oxygen carrier in its higher valence state (M_xO_y) donates lattice oxygen for fuel combustion, after which it is reduced to a lower valence state (M_xO_{y-1}), producing CO_2, H_2O, CO, H_2, or other oxidized forms of the hydrocarbon feedstock [27]. The reduced oxygen carrier (M_xO_{y-1}) is then oxidized by CO_2, H_2O, or air to its higher valence states (M_xO_y) and regenerated for the next oxidation half-cycle. Compared to transitional chemical reactor technologies, the need for product separation is minimized. In addition to inherent product separation, chemical looping technology also brings advantages in terms of additional degree of freedoms in reactant activation, circumvention of thermodynamic

equilibrium limitations that are commonly seen in conventional reactors, precise control of redox environment especially for reactions requiring mild oxidation conditions, and higher exergy efficiencies [28, 29].

It is apparent from the description above that the oxygen carrier is a critical component of the chemical looping technology. For sustained operation, oxygen carriers must withstand cyclic phase changes at high temperatures, while maintaining their activity over a long period of time. Iron-based oxides have been widely used as oxygen carriers in chemical looping processes owing to their high activity, environmentally friendly nature, and low cost [30–34]. However, their low mechanical strength and rapid degradation caused by sintering and agglomeration in high temperature operations limit their overall performance [35]. Therefore, improving the performance of iron-based oxides is an important aspect in the advancement of Fe-based chemical looping technology. During the redox cycles, Fe ions in the iron-based oxygen carriers progressively migrate from the bulk to the surface, where they are enriched [36]. The ion migration also accelerates the sintering of the oxygen carriers [37]. The addition of a support material is a common strategy to inhibit sintering, as the support can physically anchor the catalyst particles, or chemically stabilize the active sites by forming new phases or alter the surface charge, reducing the driving force for solid-state diffusing and agglomerating [38]. While doping and adding supports, *e.g.*, Al_2O_3 [39], $MgAl_2O_4$ [40], CeO_2 [41, 42], ZrO_2 [43,44], have been shown to effectively retard the sintering process, the use of micro/nano-structured oxygen carriers has been proposed in recent years as a more effective approach to control and prevent sintering. Compared with conventional synthetic approaches (*e.g.*, impregnation and co-precipitation), which could aid in dispersing and stabilizing the reactive components, the development of micro-/nano structures enables the formation of well-defined physical barriers surrounding the redox-active looping agents, thus significantly improving the effectiveness of the supports, suppressing sintering or agglomeration, and increasing the cyclic durability of the oxygen carriers.

In order to improve the cyclic stability of the oxygen carriers, the structure of the oxygen carrier can be stabilized by covering the surface of the active component with a porous overlayer. Changing the components of the shell layer material can modulate key properties of the oxygen carriers, such as reactivity, mass transfer, and cycling stability. Results from previous studies indicated that the oxygen carriers with core–shell structures had satisfactory performance during chemical looping cycles. For example, Ma et al. designed an oxygen carrier with a $Fe_2O_3@CeO_2$ core–shell configuration, which exhibited significantly enhanced sintering resistance and much higher activity and stability than a Fe_2O_3/CeO_2 composite in a fixed bed for chemical looping hydrogen generation (CLHG) using CO as the fuel [45]. Liang et al. synthesized core–shell structured oxygen carriers with FeNi-based oxides as the core and TiO_2 as the shell. As a result, the active FeNi core, protected by the TiO_2, was found to have superior reactivity and steady performance for chemical looping gasification of biomass [46]. Sun et al. reported the development of novel core–shell-like Fe_2O_3/MgO microspheres for chemical looping dry reforming. Compared to Fe_2O_3/MgO particles prepared by impregnation, the core–shell microspheres exhibited higher activity and better structural stability, because the surface magnesium layer could hinder the diffusion of iron ions and effectively inhibit the enrichment of iron on the surface [47]. It is worth noting that, besides binary metal oxide system, some more complexed metal oxides could also be utilized as shell components, *e.g.*, perovskites [48]. Apart from the improvement in cycling stability that has been reported, core–shell nanostructures are considered to have other distinct advantages, such as tunable shell compositions (to render additional physical or chemical functionalities), and resistance to attrition, especially when oxygen carriers are used in fluidized beds.

In a conventional core–shell structure, where the core and shell materials are in seamless contact, the differential molar volume change of the materials upon thermal expansion and phase change would result in significant mechanical strain, which could compromise the physical integrity of the core–shell structure. Another side effect of this close contact is the formation of a new phase between the core and the shell (*e.g.*, iron silicates forms in the $Fe@SiO_2$ structure), which is often inert and leads to a decay in redox activity [49]. Moreover, as the process of coating a layer of shell precursor is often involved in the encapsulation of the nano-sized core, it remains challenging to synthesize well-defined core–shell structure, with uniform overall particle size distribution, uniform core particle sizes, uniform shell thickness, and high dispersion. Accordingly, our work proposes an approach to mitigating the mechanical stress and strain expected of core-shell structured oxygen carriers by reserving sufficient physical gap between the core and the shell, effectively forming a yolk–shell structure to accommodate the differential volumetric changes without inducing significant strain. Additionally, the yolk–shell structure could improve the redox activity of the oxygen carrier by reducing the contact between the active core and the shell, preventing irreversible solid reactions that could otherwise hinder the regeneration of the redox-active phase. Furthermore, one could fine-tune the synthesis parameters and optimize the properties (*e.g.*, thickness and porosity) of the shell towards unhindered mass transfer and satisfactory reaction kinetics.
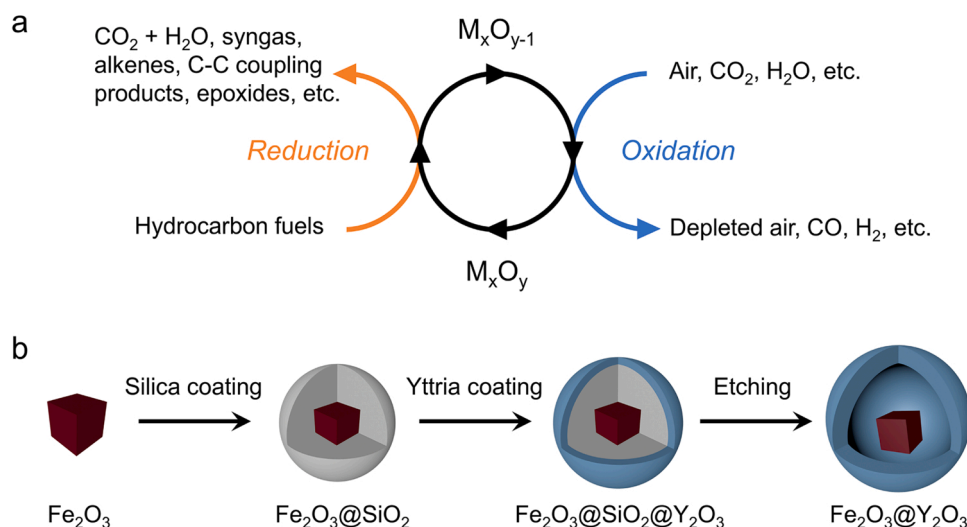

Fig. 1. Schematic illustration of the (a) chemical looping process and (b) synthesis procedure of the $Fe_2O_3@Y_2O_3$ yolk−shell oxygen carriers.

Metal oxides with high Tammann temperatures, *e.g.*, Y_2O_3, are considered to be ideal shell materials because of their superior thermal stability [50]. Herein, oxygen carriers with $Fe_2O_3@Y_2O_3$ yolk–shell nanostructure have been prepared by a coating-etching synthesis approach, as illustrated in Fig. 1b. The performance of the $Fe_2O_3@Y_2O_3$ yolk–shell nanostructures for chemical looping applications was demonstrated over 50 redox cycles in a thermogravimetric analyzer (TGA). In addition, controlled experiments, using $Fe_2O_3@Y_2O_3$ yolk–shell nanostructures with varied surface morphology and shell porosity, were performed to verify the structure-function relationship of the nanostructured oxygen carriers. The development of this yolk–shell nanostructure introduces new possibilities for the development of advanced, multifunctional, and high-performance oxygen carriers.

2. Experimental section

2.1. Material preparation

Raw materials including iron(III) nitrate nonahydrate, yttrium(III) nitrate hexahydrate, polyvinylpyrrolidone (PVP, average M_w ~29,000), hexadecyltrimethylammonium bromide (CTAB), tetraethyl orthosilicate (TEOS), sodium hydroxide, urea, N,N-dimethylformamide (DMF), ammonium hydroxide solution (~30%), cyclohexane, and absolute ethanol were purchased from Sigma-Aldrich and used without further purification.

2.1.1. Synthesis of Fe_2O_3 nanocubes (FNC)

The synthesis of Fe_2O_3 nanocubes is adapted from a procedure reported by Zheng et al [51]. In a typical synthesis, 0.404 g of Fe $(NO_3)_3 \cdot 9 H_2O$ and 0.6 g of PVP were dissolved in 36 mL DMF in a 100 mL autoclave, which was then heated to 180 °C for 30 h. The resulting nanoparticles were washed with 30 mL ethanol for 3 times (8000 rpm, 10 min) and redispersed in 45 mL of ethanol.

2.1.2. Synthesis of $Fe_2O_3@SiO_2$ nanospheres with smooth surface (Fe@s-Si)

A suspension of the as-prepared FNC in 45 mL ethanol was mixed with 15 mL H_2O and 3 mL $NH_3 \cdot H_2O$. Then 10 mL of TEOS in ethanol (10 vol%) was added dropwise to the aforementioned Fe_2O_3 suspension and stirred at room temperature for 12 h. The resulting nanoparticles were washed with 30 mL ethanol for 3 times (8000 rpm, 10 min).

2.1.3. Synthesis of $Fe_2O_3@SiO_2$ nanospheres with rough surface (Fe@r-Si)

100 mg of FNC was dispersed in 50 mL H_2O by sonication. Afterward, 1.0 g of CTAB and 0.8 mL of NaOH (0.1 M) were added to the solution and stirred gently at 60 °C for 2 h, then 20 mL of TEOS in cyclohexane (20 vol%) was added to the solution and kept at 60 °C in an oil bath with magnetic stirring for 72 h. The obtained products were washed with DI water for 3 times (8000 rpm, 10 min).

2.1.4. Synthesis of $Fe_2O_3@SiO_2@Y_2O_3$ nanospheres with smooth or rough surface (Fe@s-Si@s-Y and Fe@r-Si@r-Y)

200 mg of $Fe_2O_3@SiO_2$ nanospheres, 155 mg of $Y(NO_3)_3 \cdot 6 H_2O$, and 2.1 g of urea were dispersed or dissolved in 200 mL H_2O and heated to 90 °C for 2 h. The obtained products were washed with DI water for 3 times (8000 rpm, 10 min), dried overnight at 80 °C in an oven, and calcined in a muffle furnace at 800 °C (heating rate of 2 °C/min) for 3 h.

2.1.5. Synthesis of $Fe_2O_3@Y_2O_3$ yolk–shell nanospheres with smooth or rough surface (Fe@s-Y and Fe@r-Y)

The silica layer was etched out of the nanostructures by washing the $Fe_2O_3@SiO_2@Y_2O_3$ nanospheres with 100 mL NaOH solution (1 M) at 50 °C for 24 h. The obtained products were washed with DI water for 3 times (8000 rpm, 10 min), and dried overnight at 80 °C in an oven.

2.1.6. Synthesis of $Fe_2O_3@Y_2O_3$ yolk–shell nanospheres with cracked shell

In a typical preparation of the cracked nanostructure, 1 g of yolk–shell oxygen carriers were mixed with 2 mL ethanol and transferred to a planetary ball mill (Retsch PM 100). The mixture was subsequently ball milled for 30 min at 500 rpm. The resulting products were dried at 70 °C overnight.
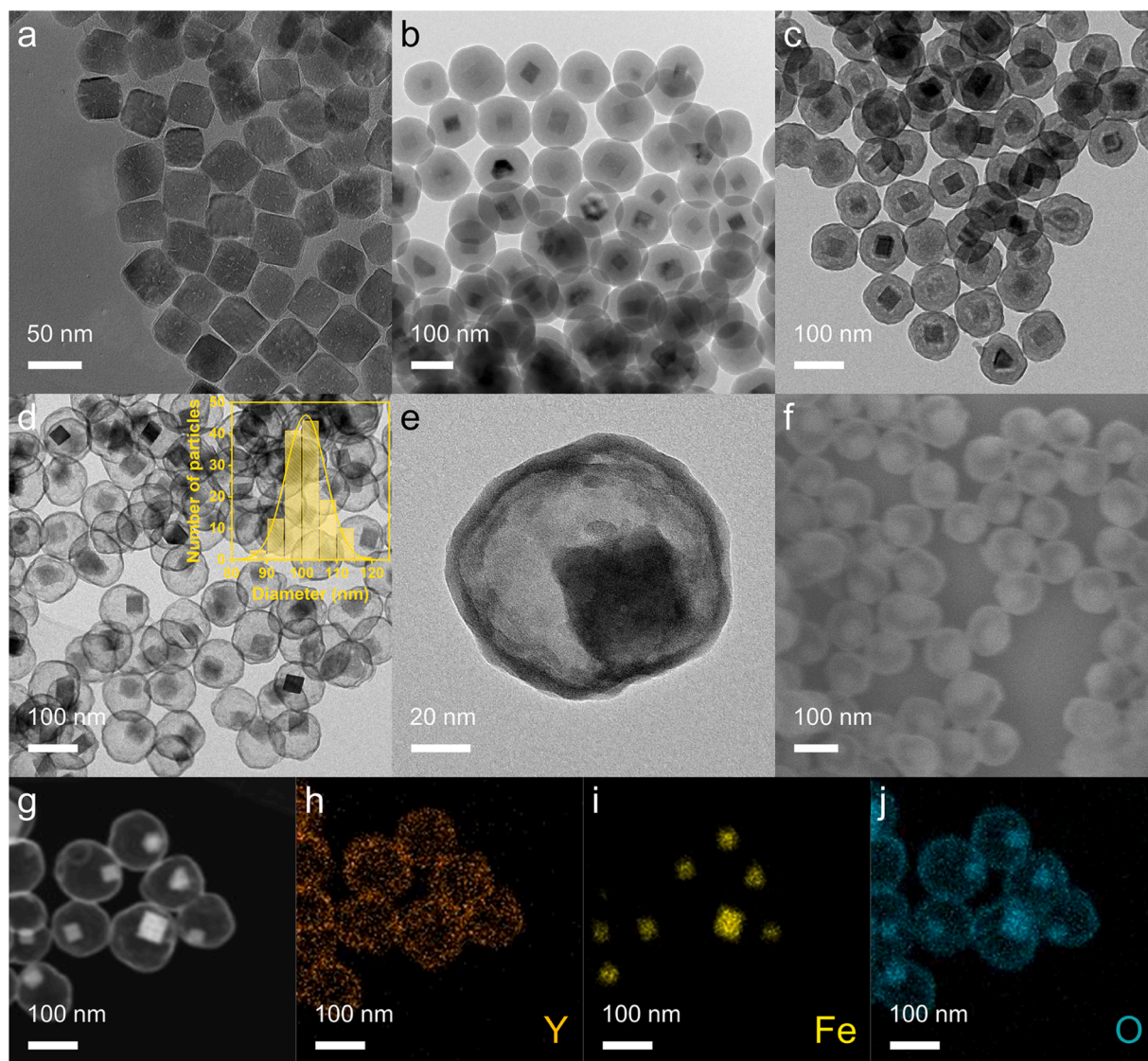
2.2. Material characterization

The crystalline phase compositions of the oxygen carriers were studied by powder X-ray diffraction (XRD) in a Bruker D8 Advance diffractometer with filtered Cu Kα radiation ($\lambda = 1.5418$ Å) at 40 kV and 40 mA. The XRD patterns were collected with 2θ range from 10° to 90°, a step size of 0.02°, and a collection time of 1 s/step. Transmission electron microscopy (TEM), dark field scanning transmission electron microscopy (STEM), and elemental mapping images were obtained on a JEOL 2100Plus transmission electron microscope equipped with energy dispersive spectroscopy (Oxford Instruments) at an accelerating voltage of 200 kV. The morphologies of the samples were examined by a field emission scanning electron microscope (FESEM, JEOL JSM-7600) operating at 15 kV. To examine the ultimate thermal stability of the oxygen carriers and the mechanism of thermal deactivation, *in situ* TEM and selected area electron diffraction (SAED) were performed in an aberration corrected JEOL ARM200CF microscope equipped with a cold field-emission gun operating at 200 kV. Protochips Atmosphere 210 gas cell system allows for dynamic observation of materials under atmospheric pressure inside the TEM column. During the experiment, the electron dose rate was kept below 300 e/Å²s at all times. Before the reactive gas was introduced into the gas cell, the sample was first heated at a rate of 1 °C/s to a target temperature in 760 Torr of Ar. The images and SAED pattern were collected while 760 Torr of pure H_2 or synthetic air (20% O_2 in N_2) was flowing over the sample with a nominal flow rate of 1 mL/min. Specific surface areas were determined from nitrogen adsorption/desorption isotherms, measured on a Micromeritics 3Flex BET system. The samples were degassed in vacuum at 150 °C for 12 h before the isotherm measurements. Temperature-programmed reduction experiments in H_2 (H_2-TPR) were performed using Micromeritics AutoChem II 2920 equipped with a thermal conductivity detector (TCD) to analyze the reduction behavior of the yolk–shell structured oxygen carriers. In a typical H_2-TPR experiment, ~40 mg of sample was first degassed at 150 °C in Ar (50 mL/min) for 60 min, followed by a temperature ramp from 100 to 900 °C in 5% H_2/Ar (50 mL/min) at a rate of 3 °C/min. The elemental compositions of oxygen carriers were quantified by inductively coupled plasma optical emission spectrometry (ICP-OES, Agilent 5800). In a typical analysis, ~12 mg of precisely weighed sample was digested in 10 mL of aqua regia. The digested sample was filtered and diluted to 1000 mL in a volumetric flask before being analyzed by ICP-OES. Thermogravimetric analysis (TGA/DSC2, Mettler Toledo) was performed to determine the redox activity and stability of the oxygen carriers. In a typical analysis, ~30 mg of sample was placed in a 150 μL alumina crucible and subjected to redox cycles at 600 °C in alternating gas environments of: 5 min of N_2 (purge), 20 min of 5% H_2/N_2 (reduction), 5 min of N_2 (purge), and 10 min of air (oxidation). The total flow rate of the reactive gas entering the TGA chamber was maintained at 100 mL/min.

3. Results and discussion

3.1. Characterization of the yolk–shell structured oxygen carriers

As illustrated in Fig. 1, the procedure for synthesizing yolk–shell $Fe_2O_3@Y_2O_3$ nanoparticles consists of three main steps. Firstly, monodispersed Fe_2O_3 nanocubes (FNC) with an average particle size of 40 nm were prepared by a solvothermal reaction, as shown in Fig. 2a. Larger Fe_2O_3 nanoparticles could be obtained by increasing the solvothermal reaction time at 180 °C (*i.e.*, beyond 30 h), with the side effect of losing

Fig. 2. Morphological characterization of the prepared nanostructures. TEM images of (a) FNC, (b) Fe@s-Si, (c) Fe@s-Si@s-Y, (d) and (e) Fe@s-Y. Size distribution plot of Fe@s-Y was obtained from TEM analysis. (f) SEM, (g) HAADF-STEM, and (h-j) elemental mapping images of Fe@s-Y.

the uniformity in particle size and the cubic particle morphology (data not shown here). Then, the FNCs were coated with a layer of SiO_2 with an average thickness of about 25 nm by the Stöber method, producing $Fe_2O_3@SiO_2$ (Fe@s-Si) particles with diameter of ~90 nm (Fig. 2b). In the next step, a uniform Y_2O_3 overlayer was formed by the hydrolysis of yttrium(III) nitrate in the presence of urea and deposited onto the surface of $Fe_2O_3@SiO_2$ particles, followed by thermal treatment of the resulting products at 800 °C. The weak hydrolysis of the yttrium ions enables a slow and controllable coating [52], producing a uniform yttria shell with thickness of ~6 nm (Fig. 2c). In principle, the thickness of the yttria shell could be adjusted by varying the amount of yttrium precursor used during the preparation. The core@shell@shell ($Fe_2O_3@$-$SiO_2@Y_2O_3$) structure was preserved after the heat treatment. Lastly, the silica layer between the FNC core and the Y_2O_3 shell was removed by etching in 1 M NaOH solution at 50 °C. As such, the proposed yolk–shell $Fe_2O_3@Y_2O_3$ nanospheres (Fe@s-Y) were successfully synthesized, as shown in Fig. 2d and e, with particle size ranging from 80 to 120 nm. The smooth surface texture of the shell can be observed from the SEM image (Fig. 2f). Because the shell is only several nanometers in thickness, it is semi-transparent to the electron beam of the SEM, resulting in the FNC core inside being also visible. The EDX analysis also confirmed the desired elemental distribution of the core (Fe and O) @ shell (Y and

O) structure, as shown in Fig. 2h-j.

To investigate the effect of shell porosity on the oxygen carriers' performance, a similar yolk–shell nanostructure with a rough and porous shell was designed and synthesized using silica spheres terminated with spiky surfaces (Fe@r-Si) as the template (Fig. 3a and b), followed by the identical yttria coating and etching processes. The Fe@r-Si nanostructures with spiky surface were first synthesized by a modified epitaxial growth approach [53]. The particle size of Fe@r-Si was controlled to be similar to that of Fe@s-Si, leading to comparable interior structures, *i.e.*, similar void space between Fe_2O_3 and Y_2O_3 in the final yolk–shell structures. The silica spikes protruding from the spherical silica bases are ~10 nm in length and ~8 nm in width, as shown in Fig. 3b. After the subsequential coating of yttria and the removal of silica, the yolk–shell nanostructure (Fe@r-Y) having a mesoporous shell was obtained with well-defined morphology and uniform particle sizes (Fig. 3d-f).

The crystal structure of the as-prepared oxygen carriers was probed by XRD, as shown in Fig. 4. In all the Fe-containing oxygen carrier samples, the position and relative intensity of main diffraction peaks match well with standard hematite (JCPDS card no. 33–0664), with characteristic peaks of α-Fe_2O_3 at 24.1°, 33.1°, 49.4°, and 64° belonging to (012), (104), (024), and (300) crystal planes, respectively, confirming
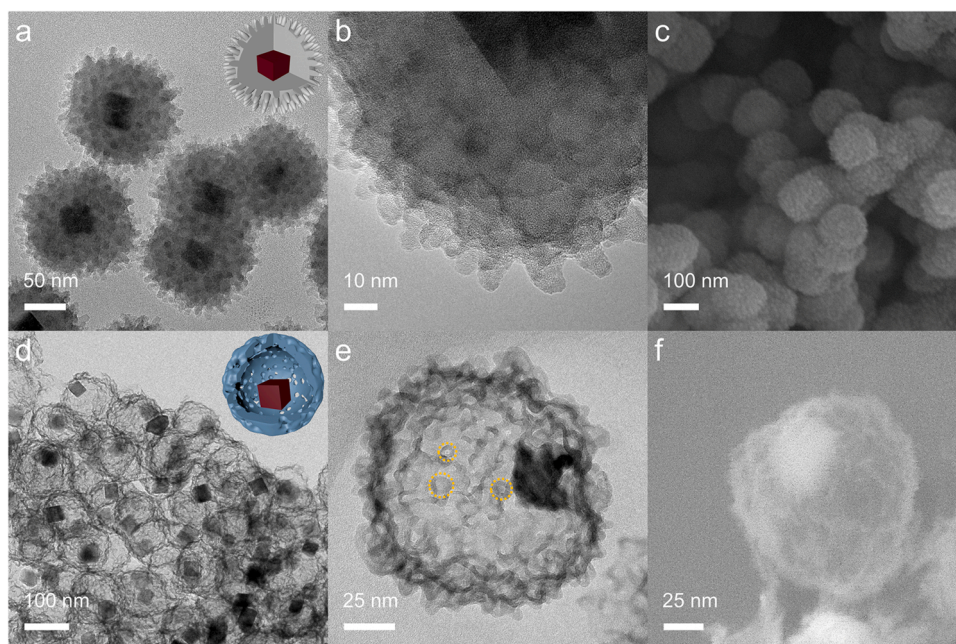
Fig. 3. Morphological characterization of the prepared nanostructures using silica template with rough surface. TEM images of (a) and (b) Fe@r-Si, (d) and (e) Fe@r-Y. SEM images of (c) Fe@r-Si, and (f) Fe@r-Y. The dashed circles highlight the top view of the nanochannels on the shell.
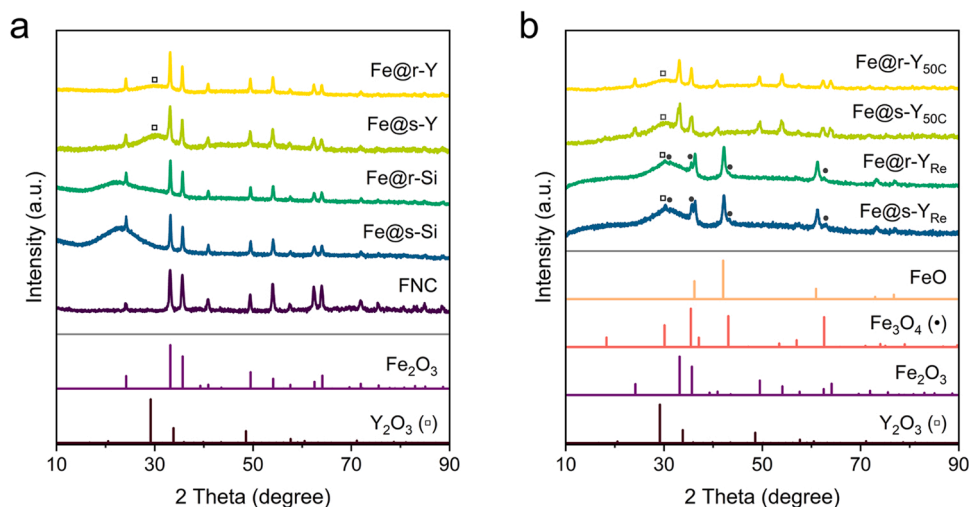

Fig. 4. XRD patterns of (a) the synthesis templates and prepared oxygen carriers, (b) the spent yolk–shell oxygen carriers at different stages during the TGA redox cycles. JCPDS card no. of reference patterns: 74–1886 (FeO), 19–0629 (Fe_3O_4), 33–0664 (Fe_2O_3), 41–1105 (Y_2O_3).

that the FNC (core) is in the α-Fe_2O_3 phase (hematite). The XRD patterns of samples with amorphous silica (Fe@s-Si and Fe@r-Si) show only a broad peak around 22°, in agreement with the typical profile of nano-sized silica [54]. This broad peak disappeared in the Fe@s-Y and Fe@r-Y samples after base etching, indicating the successful removal of the amorphous silica. Interestingly, the Y_2O_3 shell was observed to have poor crystallinity even after high temperature calcination, which could also be seen in the TEM results (Fig. 2e). For the Fe@s-Y and Fe@r-Y samples, only a broad peak around 29° (marked with square symbols) could be observed, which is assigned to the (222) plane of Y_2O_3.

The H_2 temperature programmed reduction (H_2-TPR) profiles, which characterize the lattice oxygen activity of the yolk–shell oxygen carriers, are shown in Fig. 5a. Generally, TPR peaks at lower temperatures indicate higher lattice oxygen activity. The FNC shows similar H_2-TPR profiles as that of bulky Fe_2O_3 [4], with the first reduction peak between 300 and 400 °C ($Fe_2O_3-Fe_3O_4$ transition) and the second broad peak

between 400 and 650 °C ($Fe_3O_4-FeO-Fe$ transition). To thoroughly investigate the reduction behavior of the core@shell nanostructure, Y_2O_3 hollow spheres (YHS) were also prepared using the identical synthesis method without the FNC core, as exemplified by the TEM image in Fig. 5b. The H_2-TPR profile of YHS shows that it is nearly redox-inert in the temperature range of 100–900 °C, in agreement with other yttria supports that have been previously studied [55,56]. As no phase or composition change could occur in Y_2O_3 during reduction in 5% H_2, the redox-inert behavior makes Y_2O_3 an ideal shell material. Moreover, the absence of any TPR peaks from YHS also confirms that the peaks in Fe@s-Y and Fe@r-Y samples originated from the redox-active FNC core only. The two samples with yolk–shell nanostructure, however, exhibit different TPR profiles compared with the uncoated FNC. For the yolk–shell samples, three peaks could be observed in the temperature range of 400–900 °C, which could be assigned to the $Fe_2O_3-Fe_3O_4$, Fe_3O_4-FeO, and FeO–Fe transitions, respectively. The broad peak in
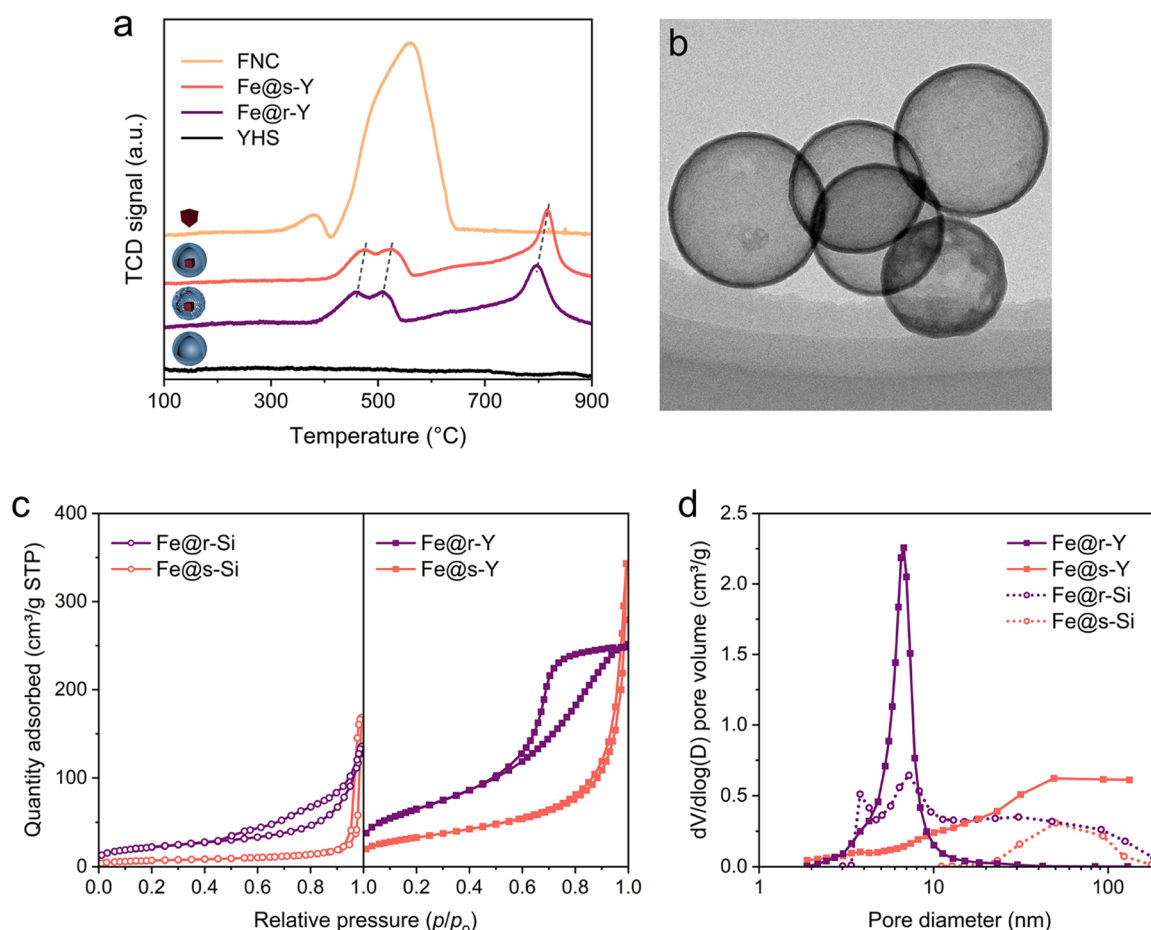
Fig. 5. (a) H$_2$-TPR profiles of the FNC, Y$_2$O$_3$ hollow spheres (YHS) and yolk–shell nanostructured oxygen carriers. (b) TEM image of YHS. (c) Nitrogen adsorption-desorption isotherms and (d) Pore diameter distribution of the silica templates and yolk–shell oxygen carriers.

FNC (400–650 °C) representing the Fe$_3$O$_4$–FeO–Fe transition could no longer be observed. Instead, both yolk–shell oxygen carriers exhibit a stepwise reduction behavior, which is attributed to the presence of the Y$_2$O$_3$ shell. Specifically, two broad peaks between 400 and 550 °C are assigned to the reduction from Fe$_2$O$_3$ to FeO, whereas the peak in the region of 780–800 °C is attributed to the reduction from FeO to metallic Fe. The redox-inert shell may have hindered the reduction of the FNC core in H$_2$ by reducing the local H$_2$ partial pressure inside the yolk–shell nanostructure, thus shifting the TPR peaks to a higher temperature range. More interestingly, all TPR peaks of Fe@r-Y appear at lower temperatures than those of Fe@s-Y, as indicated by the dashed lines in Fig. 5a. This suggests the increased porosity and consequently improved gas permeability through the yttria shell of Fe@r-Y, *i.e.*, the mass transfer across a yolk–shell structured oxygen carrier could be improved by properly tuning the shell morphology.

The surface areas of the oxygen carriers were also determined by nitrogen adsorption-desorption analysis (results summarized in Table S1 and Fig. 5). Specifically, BET analysis revealed a significant increase in surface area after the surface modification of the silica template (24.89 m^2/g for Fe@s-Si versus 79.29 m^2/g for Fe@r-Si). As a result, the yttria-coated samples follow the same trend, with Fe@r-Y exhibiting a BET specific surface area double that of Fe@s-Y. The specific surface areas of the yolk–shell nanostructures are significantly higher than those of the corresponding templates, as the result of the effective removal of silica and the creation of pore volumes (*i.e.*, the void space between the core and the shell). More interestingly, the templates and yolk–shell structured oxygen carriers with different surface morphology also possessed different adsorption-desorption behavior, as could be seen in the isotherms (Fig. 5c). Fe@s-Si and Fe@s-Y with smooth surface

morphology both exhibited Type II isotherms, corresponding to nonporous structures [57]. On the other hand, Type IV isotherms with hysteresis loops were observed in the samples with porous surface (Fe@r-Si and Fe@r-Y), indicating the mesoporous structure as expected [58]. The Type H3 (Fe@r-Si) and H2 (Fe@r-Y) hysteresis loops could be attributed to slit-like shape pores and narrow channels (ink-bottle pores), respectively, in agreement with the proposed structure design and the TEM characterization results [59]. Moreover, pore diameter distribution curves showed peaks around 8–10 nm for Fe@r-Si and Fe@r-Y, also validating the nanochannels present on the spiky surface of the oxygen carriers. The surface area measurements confirmed the mesoporous structure of designed yolk–shell nanostructures and indicate an enhanced mass transfer through the mesoporous shell of Fe@r-Y, consistent with the hypothesis during material design.

The elemental compositions of the yolk–shell oxygen carriers were characterized by ICP analysis, as summarized in Table S2. Although synthesized by two different methods, Fe@s-Y and Fe@r-Y exhibited similar elemental compositions, both containing ~36 wt% of Fe$_2$O$_3$ as the redox active component. The redox activity of the oxygen carriers could also be predicted based on the elemental composition, assuming that the lattice oxygen activity arises from the reduction of Fe$_2$O$_3$ to different valance states (Fe$_3$O$_4$ or FeO). Fe@s-Y and Fe@r-Y were estimated to possess identical oxygen carrying capacities of 1.2 wt% and 3.6 wt% in case of Fe$_2$O$_3$–Fe$_3$O$_4$ and Fe$_2$O$_3$–FeO transitions, respectively.

3.2. Oxygen carrier performance over chemical looping

The redox performance of the oxygen carrier was evaluated by

simulated chemical looping cycles at 600 °C in a TGA, with 5% H_2 in N_2 and air as the model reductant and oxidant, respectively. The operation temperature of 600 °C is chosen based on the H_2-TPR results shown in Fig. 5a, which suggests that the Fe_2O_3–FeO transition could be fully completed at 600 °C. In each cycle the sample was reduced in 5% H_2 for 20 min and re-oxidized in air for 10 min with N_2 purge (5 min) separating the two reactive segments. The relative mass changes of the oxygen carriers during the 50 redox cycles are shown in Fig. 6a and b, and the derived oxygen carrying capacity is plotted in Fig. S1. The Fe@s-Y oxygen carrier exhibited a consistent oxygen carrying capacity of ~3 wt% over 50 consecutive redox cycles, without any notable activity loss. The oxygen carrying capacity of Fe@r-Y, however, gradually decreased from ~3.2 wt% to ~2.6 wt% over the cycles. The oxygen carrying capacities of both samples are lower than the stoichiometrically calculated value of 3.6 wt%, meaning that the redox-active Fe_2O_3 could not be fully reduced to an oxidation state of Fe^{2+} (equivalent to FeO). In fact, this could be further explained by analyzing the detailed weight loss curve and redox behavior of the CLC experiments. As shown in Fig. 6c and d, during the reduction stage, the oxygen carriers were rapidly reduced to the valence state corresponding to Fe_3O_4 within one minute, followed by a relatively slow reduction to FeO. The fast reduction from Fe_2O_3 to Fe_3O_4 at the initial reduction stage (highlighted in gray color in Fig. 6c and d) could be confirmed by analyzing the mass change data, as the mass of the sample dropped to ~98.8% and the 1.2% weight loss is in agreement with the predicted value based on elemental analysis (the Fe_2O_3–Fe_3O_4 transition corresponds to a weight change of 1.2%). The first reduction stage was followed by a relatively slower reduction to FeO, which could not be completed within the 20 min in the TGA. As shown in the weight loss curves, for both Fe@s-Y and Fe@r-Y,

the sample mass decreased from ~98.8% to ~97% without reaching a steady state, leading to a total oxygen carrying capacity of ~3 wt%. No distinct steps representing the further reduction from FeO to Fe can be observed. During the oxidation with air, the sample mass quickly increased within 1–2 min to its initial value before reduction (~100%), indicating complete regeneration of the oxygen carriers. Formation of the FeO phase is also confirmed by XRD analysis of the samples collected after the reduction half cycle (Fe@s-Y_{Re} and Fe@r-Y_{Re}), as shown in Fig. 4b, with minor presence of the Fe_3O_4 phases (marked with black dots). The XRD results also reveal that the phase transition of Fe_2O_3–Fe_3O_4–FeO is unaffected by the yttria shell. No mixed oxide phase was observed, other than the binary oxides of iron and yttrium, suggesting the absence of chemical reaction between the Y_2O_3 shell and the redox-active Fe_2O_3 core during the redox cycles.

The difference in the redox behavior of the oxygen carriers was further analyzed to investigate the impact of the surface morphology and the structure-function relationship. The two yolk–shell oxygen carriers, despite having identical elemental compositions, i.e., same amount of redox-active Fe_2O_3, showed slightly different oxygen carrying capacities in the 50 redox cycles (3.0 wt% for Fe@s-Y versus 3.2 wt% for Fe@r-Y), probably owing to the higher permeability of H_2 across the mesoporous shell of Fe@r-Y. In this case, the FNC cores in Fe@r-Y could be reduced to a valance state closer to Fe^{2+} (FeO), resulting in a higher reactivity than Fe@s-Y. The deep reduction of Fe@r-Y cf. Fe@s-Y could also be confirmed by XRD results, as shown in Fig. 4b, where reduced Fe@r-Y (Fe@r-Y_{Re}) possessed lower amount of Fe_3O_4 than reduced Fe@s-Y (Fe@s-Y_{Re}) according to the peak intensities of the Fe_3O_4 and FeO diffraction peaks. Accordingly, Fe@r-Y also exhibited a higher reaction rate than Fe@s-Y, as shown by the mass change curves during the
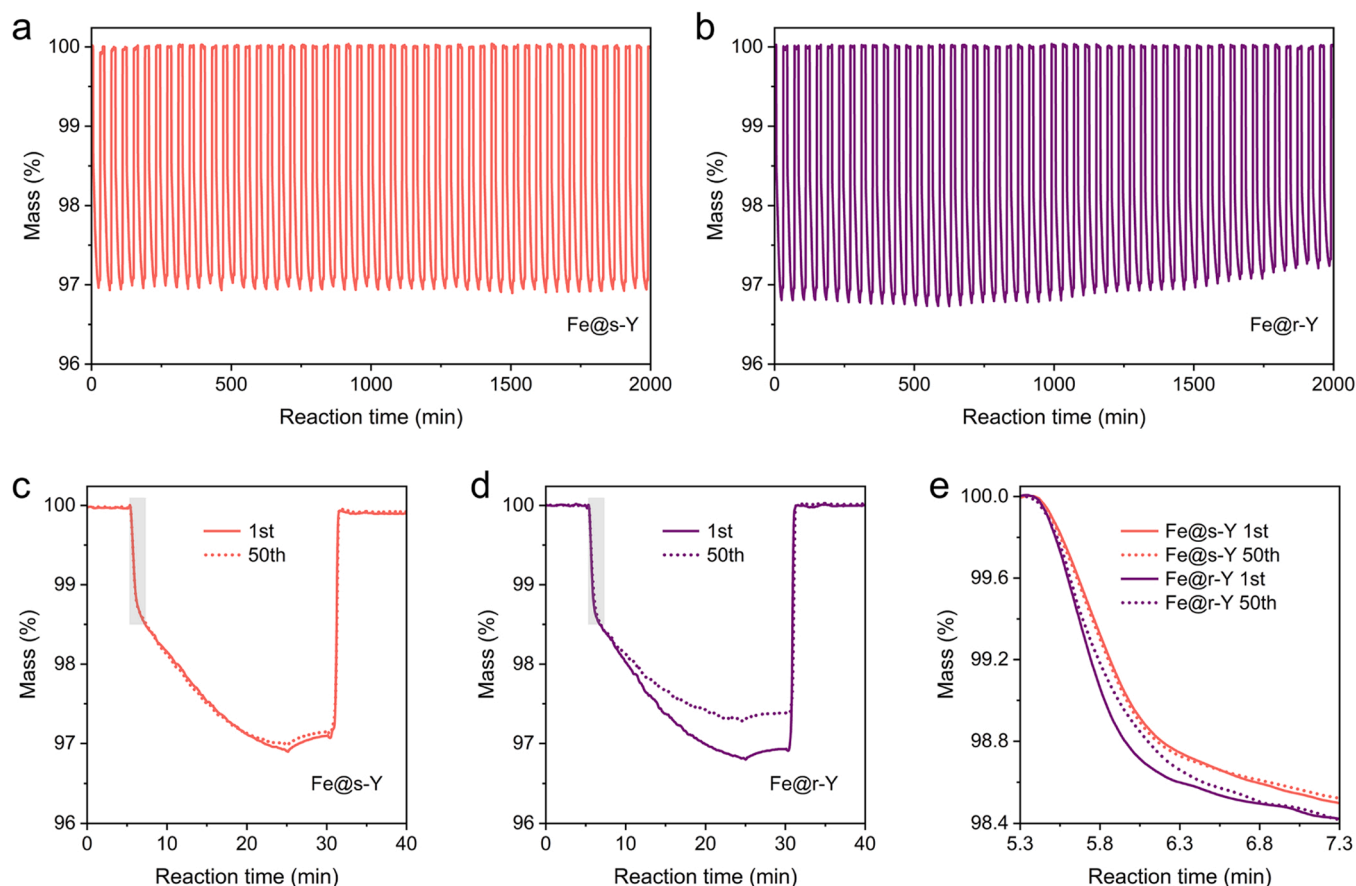
Fig. 6. Redox cycling performance of the yolk–shell oxygen carriers. Mass change of (a) Fe@s-Y and (b) Fe@r-Y during 50 TGA redox cycles. Comparison of mass change curve during the first and 50th redox cycles for (c) Fe@s-Y and (d) Fe@r-Y. (e) Enlarged mass change curve during the initial reduction stage (highlighted in gray color in c and d).

initial reduction stage (Fig. 6e). During the first cycle, the rapid reduction from Fe_2O_3 to Fe_3O_4, which corresponds to a mass change of 1.2% could be completed within ~6.0 min and ~6.2 min for Fe@r-Y and Fe@s-Y, respectively, followed by a much slower reduction to FeO. After 50 cycles, the reduction kinetics of Fe@s-Y was indistinguishable from that in the first cycle, while the reduction rate of Fe@r-Y exhibited a minor decay. The difference in the reaction rate may be attributed to the sample morphology, *i.e.*, a porous yttria shell corresponds to faster mass transfer through the shell and therefore faster reduction kinetics.

Therefore, the results above show that mass transfer during the redox reaction is dominated by pore diffusion when the Y_2O_3 shells are mesoporous. When the mesoporosity of the Y_2O_3 shells has significantly reduced, *e.g.*, in the case of Fe@s-Y and the cycled Fe@r-Y, the diffusion through the pores in the Y_2O_3 shells would correspondingly reduce, resulting in slightly reduced apparent rates. On the other hand, although Y_2O_3 is known to possess oxygen vacancies and exhibit considerable ionic conductivity at and above 600 °C [60–62], the rate of ionic diffusion through a solid Y_2O_3 shell is expected to be slow compared to that of molecular diffusion through the pores.

The morphology of yolk–shell oxygen carriers after redox cycles were characterized by TEM to investigate their structural stability. The spent samples after 5, 20, and 50 redox cycles in TGA were collected for analysis. The evolution of sample morphology with increasing reaction time was clearly observed, as shown in Fig. 7. After 5 cycles, the particle morphology of most FNC cores in Fe@s-Y deviated slightly from the cubic form, probably owing to the cyclic phase change between Fe_2O_3 and FeO. After 20 cycles, most of the FNC cores no longer retained their cubic form, while remaining somewhat granular. By the end of the 50th redox cycle, some of the FNC cores in Fe@s-Y appeared disintegrated and were attached to the shell walls. Interestingly, although the cores gradually became adhered to the shells over redox cycles, a clear boundary between the Fe_2O_3 and Y_2O_3 could still be observed (Fig. S2). The yttria shells were found to remain amorphous even after 50 cycles, in agreement with XRD results shown in Fig. 4b. Similarly, the Fe@r-Y oxygen carriers demonstrated comparable structural stability over the redox cycles. Minor shell fragmentation and the resulting exposure of FNC cores, however, could be observed for Fe@r-Y, probably owing to the compromised toughness of the highly porous yttria shell. The partial fracture of the yttria shells may also account for the slight deactivation

observed by the cycling experiments in TGA. Considering that the majority of the shells remain structurally intact, it could be concluded that in both yolk–shell nanostructures (Fe@s-Y and Fe@r-Y), the yttria shells withstood the thermochemical redox cycles and maintained their structural integrity, isolating and protecting the redox-active cores from sintering and agglomeration. The surface areas of the spent oxygen carriers were also measured to evaluate their mesoporosity, as summarized in Table S1. The BET surface areas of Fe@s-Y and Fe@r-Y were determined to be 85 and 189 m^2/g, respectively. Compared with the fresh samples, the cycled Fe@s-Y and Fe@r-Y samples (after 50 redox cycles) both exhibited some extent of loss of porosity (a 20–30% decrease). Nevertheless, their cycling performance was almost unaffected.

In the yolk–shell oxygen carriers, the thermally stable yttria shell forms a continuous physical barrier that exerts maximum Zenner pinning force to resist the sintering of the active core. To verify the superiority of the yolk–shell design and the necessity for having a continuous physical barrier in preserving the morphology of the oxygen carriers, the yttria shells of the Fe@r-Y oxygen carriers were mechanically fractured by high energy ball milling, resulting in physically compromised yolk–shell structures, as shown in Fig. 8a and b. The mechanical force in the ball milling led to shell fragmentation, exposing the FNC cores to the redox atmosphere as highlighted in the dashed square in Fig. 8b. The resulting sample was then subjected to 10 redox cycles under the same reaction condition in TGA (results shown in Fig. 8d) Cracked-shell sample showed obvious activity loss over 10 redox cycles, after which all features of the original yolk–shell morphology were completely lost, indicating severe sintering and agglomeration of the redox-active FNC, as shown by TEM image in Fig. 8c. This control experiment corroborates the importance of having intact shells for maximum sintering resistance and cyclic stability. The experimental results discussed above unequivocally demonstrate the importance of selecting suitable shell material (*e.g.*, Y_2O_3) and designing appropriate nanostructure to overcome sintering and deactivation of Fe_2O_3-based oxygen carriers, without sacrificing the reaction rates or inducing unfavorable chemical interactions between the redox-active components and the support material.
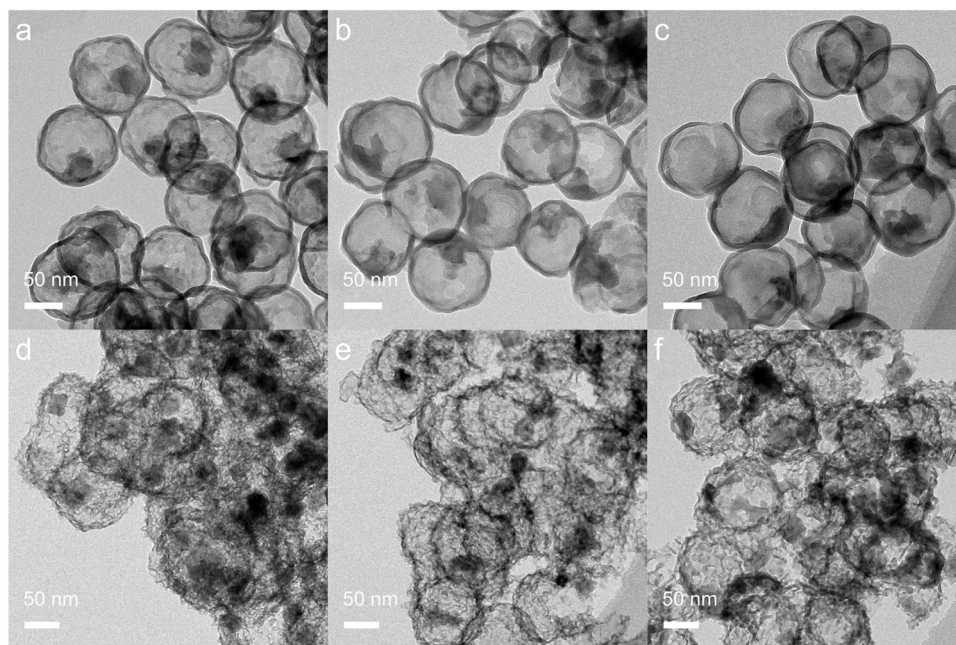
Fig. 7. TEM images of Fe@s-Y oxygen carriers after (a) 5, (b) 20, and (c) 50 redox cycles and Fe@r-Y oxygen carriers after (d) 5, (e) 20, and (f) 50 redox cycles in TGA.
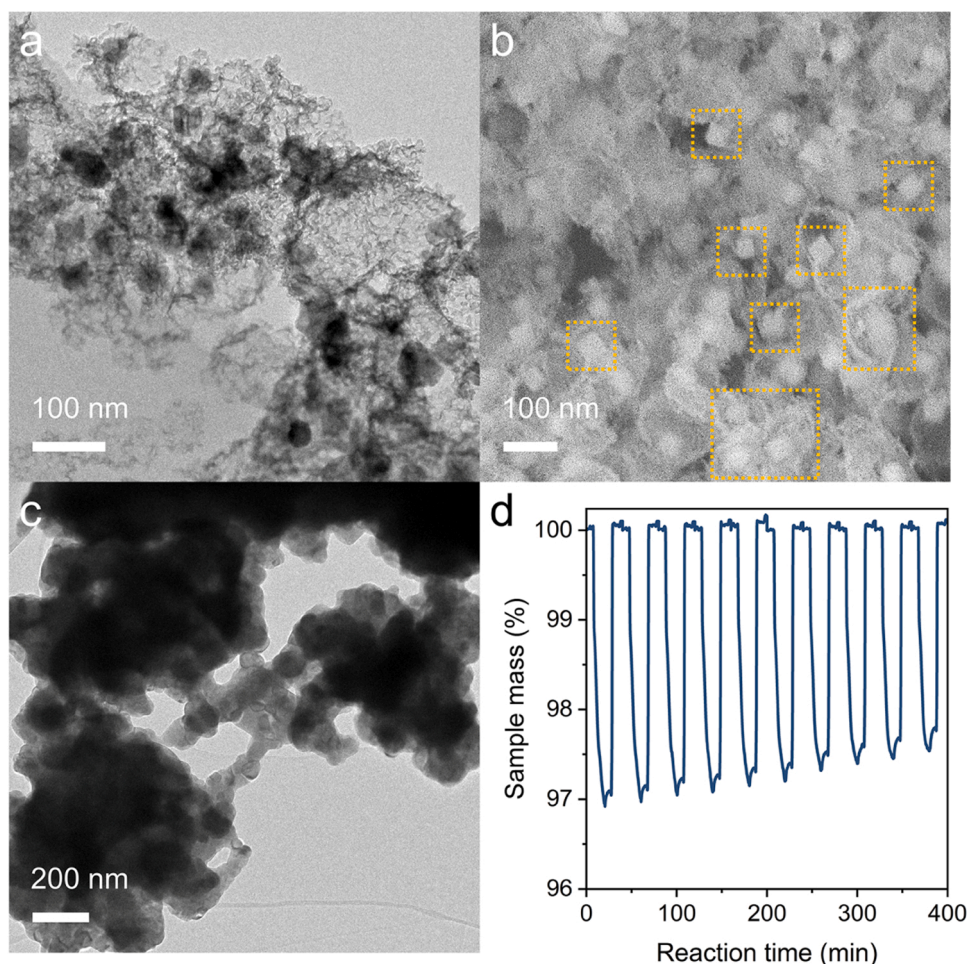
Fig. 8. Effect of yolk–shell structure on redox cycling stability. (a) TEM and (b) SEM images of the Fe@r-Y with cracked shell prepared by ball milling. (c) TEM image of the Fe@r-Y with cracked shell after TGA redox cycles. (d) Mass change of Fe@r-Y with cracked shell during 10 TGA redox cycles.

3.3. Prospects and challenges in applying yolk–shell structured oxygen carriers in practical chemical looping operation conditions

As mentioned above, the operation temperature of 600 °C is chosen based on the H_2-TPR results shown in Fig. 5a, which suggests that the Fe_2O_3–FeO transition could be fully completed at 600 °C. Although 600 °C is high for chemical looping applications such as oxidative dehydrogenation of alkanes and epoxidation, it is on the low end of operating temperatures of chemical looping applications that operate much closer to thermodynamic equilibrium, *e.g.*, combustion, gasification, and reforming. To examine the suitability of the yolk–shell oxygen carrier for redox cycles at elevated temperatures, *in situ* TEM experiments were conducted, in which the Fe@s-Y is subjected to a redox cycle at 800 °C. From the *in situ* TEM results shown in Fig. S3, it can be seen that the originally amorphous Y_2O_3 shell crystallized at 800 °C, accompanied by the apparent densification of the shell and signs of shell deformation. It is expected that such crystallization would lead to loss of porosity, reduced redox kinetics, and potentially compromised yolk-shell morphology. To this end, further systematic studies are required to further assess the suitability of yolk–shell structured oxygen carriers for high temperature operations, and to explore possible synthetic approaches to remedy the potential issues caused by Y_2O_3 crystallization.

Secondly, it should be noted that the present study focuses on the development of well-defined yolk–shell structures with the aim of addressing the problem of sintering due to high temperature and cyclic redox reactions. Accordingly, the chemical looping experiments were performed using a rather ideal reductant (fuel), *viz.*, hydrogen. In many

practical scenarios, the reductant is often a hydrocarbon fuel, whose activation requires the presence of metals or metal oxides that are more catalytically active towards C-H bond cleavage than Fe_2O_3 and Y_2O_3. With the availability of a durable structure design, such catalytic functionalities can be easily incorporated into the oxygen carrier, *e.g.*, by depositing nanoparticles of catalytically active metals or alloys in the interior or exterior of the Y_2O_3, as exemplified by our previous work on other types of multifunctional nanostructured catalysts [63]. Furthermore, the impacts of side effects associated with the use of carbonaceous fuels, such as carbon deposition, on the stability of the yolk–shell structured oxygen carriers, should be further investigated in future studies.

Another important performance criterion for oxygen carriers is their mechanical strength against particle breakage and attrition, which are particularly important when the chemical looping reactions are carried out in circulating fluidized beds. Here, although the present study did not investigate the bulk mechanical properties of the yolk–shell oxygen carriers, which were only evaluated in their powder forms, the issue of mechanical strength could be addressed in further studies. Nominally, Y_2O_3 ceramics have a hardness of 5.5 on the Mohs scale, which is still acceptable for long-term operation in fluidized beds. Therefore, conventional ceramic processing techniques, *e.g.*, controlled sintering of the yolk–shell particles to introduce slight extent of neck formation between adjacent Y_2O_3 shells, could be potentially feasible means to render physical robustness to the $Fe_2O_3@Y_2O_3$ yolk–shell oxygen carriers, when they are produced at scale in pellet forms and used in fluidized beds for chemical looping applications.

Lastly, the cost of an oxygen carrier is a crucial factor when assessing its techno-economic feasibility. Although Fe is a cheap base metal, yttrium is considered a rare-earth element, which is both rare and expensive. Additionally, the preparation of the $Fe_2O_3@Y_2O_3$ yolk–shell oxygen carriers is rather intricate, *e.g.*, the coating of SiO_2 template requires highly diluted precursor solutions to achieve control of layer thickness. Also, the preparation of the yolk–shell morphology involves a sacrificial template, which does not represent a high atom economy. The solvothermal synthesis of Fe_2O_3 is also a process that is rather expensive to scale up using conventional reactor technologies. Therefore, the economic feasibility of adopting the $Fe_2O_3@Y_2O_3$ yolk–shell oxygen carriers for large scale chemical looping operations must be carefully assessed. In the first instance, the chemical looping performance of $Fe_2O_3@Y_2O_3$ oxygen carriers must be far superior to low-cost oxygen carriers such as iron ores in terms of redox activity, cyclic stability, and robustness against attrition and impurities to justify the utility of the former. While the present study has demonstrated the possibility of preparing morphologically well-defined, nanostructured oxygen carriers with outstanding cyclic stability, substantially more development and innovation in process technology is required to bring down the cost of preparing nanostructured materials and improve their cost-competitiveness.

4. Conclusion

In summary, two $Fe_2O_3@Y_2O_3$ oxygen carriers with yolk–shell nanostructures, Fe@s-Y and Fe@r-Y, were synthesized using a coating-etching method. The highly reproducible synthesis protocol also allows fine-tuning of the shell morphology and porosity, such that the importance of surface morphology, nanostructure design, and the structure-function relationship could be systematically investigated. The resulting nanoparticle structures were confirmed by electron microscopy, followed by an evaluation of their redox performance over a simulated chemical looping cycle at 600 °C in TGA. The Fe@s-Y oxygen carrier exhibited consistent oxygen- carrying capacity of 3 wt% over 50 consecutive redox cycles, without any distinguishable structural degradation. The Fe@r-Y oxygen carrier was found to initially possess a higher reaction rate owing to the enhanced mass transfer through the mesoporous shell. Its cycling activity, however, decayed slightly as a result of the breakage of the relatively fragile porous yttria shell. The present study demonstrates, for the first time, the utilization of uniform and well-defined yolk–shell structured oxygen carriers with the ability to retain excellent structural definition over large numbers of chemical looping cycles.

CRediT authorship contribution statement

Qianwenhao Fan: Writing – review & editing, Writing – original draft, Investigation, Formal analysis, Conceptualization. **Bingqing Yao:** Writing – review & editing, Investigation, Formal analysis. **Mingwu Tan:** Writing – review & editing, Investigation, Formal analysis. **Longgang Tao:** Investigation, Formal analysis. **Syed Saqline:** Investigation, Formal analysis. **Wen Liu:** Writing – review & editing, Supervision, Conceptualization. **Qian He:** Writing – review & editing, Supervision.

Declaration of Competing Interest

The authors declare that they have no known competing financial interests or personal relationships that could have appeared to influence the work reported in this paper.

Data availability

Data will be made available on request.

Author contributions

The manuscript was written through contributions of all authors. All authors have given approval to the final version of the manuscript.

Associated content

Supporting Information Available: BET surface area and ICP analysis results, oxygen carrying capacity of the two yolk–shell structured oxygen carriers during the cycles and additional TEM images.

Appendix A. Supporting information

Supplementary data associated with this article can be found in the online version at doi:10.1016/j.apcatb.2024.123935.

References

[1] J. Hu, V.V. Galvita, H. Poelman, G.B. Marin, Advanced chemical looping materials for CO2 utilization: a review, Materials 11 (2018) 1187, https://doi.org/10.3390/ma11071187.

[2] S.C. Bayham, A. Tong, M. Kathe, L.S. Fan, Chemical looping technology for energy and chemical production, Wiley Interdiscip. Rev. Energy Environ. 5 (2016) 216–241, https://doi.org/10.1002/wene.173.

[3] S. Saqline, Z.Y. Chua, W. Liu, Coupling chemical looping combustion of solid fuels with advanced steam cycles for CO2 capture: a process modelling study, Energy Convers. Manag. 244 (2021) 114455, https://doi.org/10.1016/j.enconman.2021.114455.

[4] Q. Fan, et al., Breaking the stoichiometric limit in oxygen-carrying capacity of Fe-based oxygen carriers for chemical looping combustion using the Mg-Fe-O solid solution system, ACS Sustain. Chem. Eng. 10 (2022) 7242–7252, https://doi.org/10.1021/acssuschemeng.2c00271.

[6] A. Goel, E.M. Moghaddam, W. Liu, C. He, J. Konttinen, Biomass chemical looping gasification for high-quality syngas: a critical review and technological outlooks, Energy Convers. Manag. 268 (2022) 116020, https://doi.org/10.1016/j.enconman.2022.116020.

[7] L. Yu, et al., Developing oxygen carriers for chemical looping biomass processing: challenges and opportunities, Adv. Sustain. Syst. 4 (2020) 2000099, https://doi.org/10.1002/adsu.202000099.

[8] S. Saqline, et al., Investigation of barium iron oxides for CO2 capture and chemical looping oxygen uncoupling, Appl. Energy Combust. Sci. 17 (2024) 100238, https://doi.org/10.1016/j.jaecs.2023.100238.

[9] S. Saqline, L. Yang, A. Romagnoli, W. Liu, Coupling chemical looping air separation with the Allam cycle – a thermodynamic analysis, J. Clean. Prod. 418 (2023) 138097, https://doi.org/10.1016/j.jclepro.2023.138097.

[10] T. Xu, X. Wang, B. Xiao, W. Liu, Single-step production of hydrogen-rich syngas from toluene using multifunctional Ni-dolomite catalysts, Chem. Eng. J. 425 (2021) 131522, https://doi.org/10.1016/j.cej.2021.131522.

[11] T. Xu, X. Wang, B. Xiao, H. Zhao, W. Liu, Optimisation of syngas production from a novel two-step chemical looping reforming process using Fe-dolomite as oxygen carriers, Fuel Process. Technol. 228 (2022) 107169, https://doi.org/10.1016/j.fuproc.2022.107169.

[12] T. Xu, et al., Modulating lattice oxygen activity of Ca2Fe2O5 brownmillerite for the co-production of syngas and high purity hydrogen via chemical looping steam reforming of toluene, Appl. Catal. B Environ. 320 (2023) 122010, https://doi.org/10.1016/j.apcatb.2022.122010.

[13] S. Chen, et al., Coverage-dependent behaviors of vanadium oxides for chemical looping oxidative dehydrogenation, Angew. Chem. Int. Ed. 59 (2020) 22072–22079, https://doi.org/10.1002/anie.202005968.

[14] S. Chen, et al., Modulating lattice oxygen in dual-functional Mo–V–O mixed oxides for chemical looping oxidative dehydrogenation, J. Am. Chem. Soc. 141 (2019) 18653–18657, https://doi.org/10.1021/jacs.9b09235.

[15] Y. Gao, F. Haeri, F. He, F. Li, Alkali metal-promoted LaxSr2−xFeO4−δ redox catalysts for chemical looping oxidative dehydrogenation of ethane, ACS Catal. 8 (2018) 1757–1766, https://doi.org/10.1021/acscatal.7b03928.

[16] L.M. Neal, S. Yusuf, J.A. Sofranko, F. Li, Oxidative dehydrogenation of ethane: a chemical looping approach, Energy Technol. 4 (2016) 1200–1208, https://doi.org/10.1002/ente.201600074.

[17] Z. Cheng, et al., C2 selectivity enhancement in chemical looping oxidative coupling of methane over a Mg–Mn composite oxygen carrier by Li-doping-induced oxygen vacancies, ACS Energy Lett. 3 (2018) 1730–1736, https://doi.org/10.1021/acsenergylett.8b00851.

[18] V. Fleischer, et al., Investigation of the role of the Na2WO4/Mn/SiO2 catalyst composition in the oxidative coupling of methane by chemical looping experiments, J. Catal. 360 (2018) 102–117, https://doi.org/10.1016/j.jcat.2018.01.022.

[19] W. Sun, et al., An oxygen carrier catalyst toward efficient chemical looping-oxidative coupling of methane, Appl. Catal. B Environ. 304 (2022) 120948, https://doi.org/10.1016/j.apcatb.2021.120948.

[20] M.S.C. Chan, E. Marek, S.A. Scott, J.S. Dennis, Chemical looping epoxidation, J. Catal. 359 (2018) 1–7, https://doi.org/10.1016/j.jcat.2017.12.030.

[21] E.J. Marek, S. Gabra, J.S. Dennis, S.A. Scott, High selectivity epoxidation of ethylene in chemical looping setup, Appl. Catal. B Environ. 262 (2020) 118216, https://doi.org/10.1016/j.apcatb.2019.118216.

[22] E.J. Marek, E. García-Calvo Conde, Effect of catalyst preparation and storage on chemical looping epoxidation of ethylene, Chem. Eng. J. 417 (2021) 127981, https://doi.org/10.1016/j.cej.2020.127981.

[23] G. Voitic, V. Hacker, Recent advancements in chemical looping water splitting for the production of hydrogen, RSC Adv. 6 (2016) 98267–98296, https://doi.org/10.1039/C6RA21180A.

[24] X. Zhu, et al., Chemical-looping water splitting over ceria-modified iron oxide: performance evolution and element migration during redox cycling, Chem. Eng. Sci. 179 (2018) 92–103, https://doi.org/10.1016/j.ces.2018.01.015.

[25] B. Bulfin, M. Zuber, O. Gräub, A. Steinfeld, Intensification of the reverse water–gas shift process using a countercurrent chemical looping regenerative reactor, Chem. Eng. J. 461 (2023) 141896, https://doi.org/10.1016/j.cej.2023.141896.

[26] J. Adanez, A. Abad, Chemical-looping combustion: status and research needs, Proc. Combust. Inst. 37 (2019) 4303–4317, https://doi.org/10.1016/j.proci.2018.09.002.

[27] L. Zeng, Z. Cheng, J.A. Fan, L.-S. Fan, J. Gong, Metal oxide redox chemistry for chemical looping processes, Nat. Rev. Chem. 2 (2018) 349–364, https://doi.org/10.1038/s41570-018-0046-2.

[28] H.M. Kvamsdal, K. Jordal, O. Bolland, A quantitative comparison of gas turbine cycles with CO2 capture, Energy 32 (2007) 10–24, https://doi.org/10.1016/j.energy.2006.02.006.

[29] W. Liu, Controlling lattice oxygen activity of oxygen carrier materials by design: a review and perspective, React. Chem. Eng. 6 (2021) 1527–1537, https://doi.org/10.1039/D1RE00209K.

[30] S. Luo, L. Zeng, L.S. Fan, Chemical looping technology: oxygen carrier characteristics, Annu Rev. Chem. Biomol. Eng. 6 (2015) 53–75, https://doi.org/10.1146/annurev-chembioeng-060713-040334.

[31] F. Blaschke, M. Bele, B. Bitschnau, V. Hacker, The effect of microscopic phenomena on the performance of iron-based oxygen carriers of chemical looping hydrogen production, Appl. Catal. B Environ. 327 (2023) 122434, https://doi.org/10.1016/j.apcatb.2023.122434.

[32] Y. Kang, et al., Promoted methane conversion to syngas over Fe-based garnets via chemical looping, Appl. Catal. B Environ. 278 (2020) 119305, https://doi.org/10.1016/j.apcatb.2020.119305.

[33] D. Hosseini, P.M. Abdala, F. Donat, S.M. Kim, C.R. Mueller, Bifunctional core-shell architecture allows stable H2 production utilizing CH4 and CO2 in a catalytic chemical looping process, Appl. Catal. B Environ. 258 (2019) 117946, https://doi.org/10.1016/j.apcatb.2019.117946.

[34] D. Zeng, et al., Spatially controlled oxygen storage materials improved the syngas selectivity on chemical looping methane conversion, Appl. Catal. B Environ. 281 (2021) 119472, https://doi.org/10.1016/j.apcatb.2020.119472.

[35] W. Akram, Sanjay, M.A. Hassan, Chemical looping combustion with nanosize oxygen carrier: a review, International Journal of Environmental Science and Technology (2021). https://doi.org/10.1007/s13762-020-02840-8.

[36] D. Song, et al., Review on migration and transformation of lattice oxygen during chemical looping conversion: advances and perspectives, Energy Fuels 37 (2023) 5743–5756, https://doi.org/10.1021/acs.energyfuels.3c00402.

[37] Y. Guan, Y. Liu, X. Lin, B. Wang, Q. Lyu, Research progress and perspectives of solid fuels chemical looping reaction with Fe-based oxygen carriers, Energy Fuels 36 (2022) 13956–13984, https://doi.org/10.1021/acs.energyfuels.2c02802.

[38] Y. De Vos, et al., Development of stable oxygen carrier materials for chemical looping processes—a review, Catalysts 10 (2020) 926, https://doi.org/10.3390/catal10080926.

[39] Z. Ma, S. Zhang, Y. Lu, Activation mechanism of Fe2O3-Al2O3 oxygen carrier in chemical looping combustion, Energy Fuels 34 (2020) 16350–16355, https://doi.org/10.1021/acs.energyfuels.0c02967.

[40] G. Azimi, et al., Mn–Fe oxides with support of MgAl2O4, CeO2, ZrO2 and Y2O3–ZrO2 for chemical-looping combustion and chemical-looping with oxygen uncoupling, Ind. Eng. Chem. Res. 53 (2014) 10358–10365, https://doi.org/10.1021/ie500994m.

[41] D.D. Miller, R. Siriwardane, Mechanism of methane chemical looping combustion with hematite promoted with CeO2, Energy fuels 27 (2013) 4087–4096, https://doi.org/10.1021/ef302132e.

[42] K. Li, H. Wang, Y. Wei, D. Yan, Syngas production from methane and air via a redox process using Ce–Fe mixed oxides as oxygen carriers, Appl. Catal. B Environ. 97 (2010) 361–372, https://doi.org/10.1016/j.apcatb.2010.04.018.

[43] M.M. Tijani, A. Aqsha, N. Mahinpey, Synthesis and study of metal-based oxygen carriers (Cu, Co, Fe, Ni) and their interaction with supported metal oxides (Al2O3, CeO2, TiO2, ZrO2) in a chemical looping combustion system, Energy 138 (2017) 873–882, https://doi.org/10.1016/j.energy.2017.07.100.

[44] M. Keller, H. Leion, T. Mattisson, Chemical looping tar reforming using La/Sr/Fe-containing mixed oxides supported on ZrO2, Appl. Catal. B Environ. 183 (2016) 298–307, https://doi.org/10.1016/j.apcatb.2015.10.047.

[45] S. Ma, et al., Enhanced sintering resistance of Fe2O3/CeO2 oxygen carrier for chemical looping hydrogen generation using core-shell structure, Int. J. Hydrog. Energy 44 (2019) 6491–6504, https://doi.org/10.1016/j.ijhydene.2019.01.167.

[46] S. Liang, S. Liao, W. Li, C. Li, X. Ma, Enhanced stability of iron-nickel oxygen carriers in biomass chemical looping gasification by core-shell structure, Chem. Eng. J. 451 (2023) 138964, https://doi.org/10.1016/j.cej.2022.138964.

[47] Y. Sun, J. Li, H. Li, Core-shell-like Fe2O3/MgO oxygen carriers matched with fluidized bed reactor for chemical looping reforming, Chem. Eng. J. 431 (2022) 134173, https://doi.org/10.1016/j.cej.2021.134173.

[48] M. Lee, et al., Reverse water–gas shift chemical looping using a core–shell structured perovskite oxygen carrier, Energies 13 (2020) 5324, https://doi.org/10.3390/en13205324.

[49] S. Bhavsar, M. Najera, G. Veser, Chemical looping dry reforming as novel, intensified process for CO2 activation, Chem. Eng. Technol. 35 (2012) 1281–1290, https://doi.org/10.1002/ceat.201100649.

[50] A.M. Kierzkowska, R. Pacciani, C.R. Muller, C.O. CaO-based, 2 sorbents: from fundamentals to the development of new, highly effective materials, ChemSusChem 6 (2013) 1130–1148, https://doi.org/10.1002/cssc.201300178.

[51] Y. Zheng, et al., Quasicubic alpha-Fe2O3 nanoparticles with excellent catalytic performance, J. Phys. Chem. B 110 (2006) 3093–3097, https://doi.org/10.1021/jp056671q.

[52] F. Zhang, et al., Fabrication of Ag@SiO2@Y2O3: Er nanostructures for bioimaging: tuning of the upconversion fluorescence with silver nanoparticles, J. Am. Chem. Soc. 132 (2010) 2850–2851, https://doi.org/10.1021/ja909108x.

[53] W. Wang, et al., Facile synthesis of uniform virus-like mesoporous silica nanoparticles for enhanced cellular internalization, ACS Cent. Sci. 3 (2017) 839–846, https://doi.org/10.1021/acscentsci.7b00257.

[54] R. Maddalena, C. Hall, A. Hamilton, Effect of silica particle size on the formation of calcium silicate hydrate [CSH] using thermal analysis, Thermochim. Acta 672 (2019) 142–149, https://doi.org/10.1016/j.tca.2018.09.003.

[55] G. Sun, K. Hidajat, X. Wu, S. Kawi, A crucial role of surface oxygen mobility on nanocrystalline Y2O3 support for oxidative steam reforming of ethanol to hydrogen over Ni/Y2O3 catalysts, Appl. Catal. B Environ. 81 (2008) 303–312, https://doi.org/10.1016/j.apcatb.2007.12.021.

[56] H. Liu, D. He, Properties of Ni/Y2O3 and its catalytic performance in methane conversion to syngas, Int. J. Hydrog. Energy 36 (2011) 14447–14454, https://doi.org/10.1016/j.ijhydene.2011.08.025.

[57] M. Thommes, et al., Physisorption of gases, with special reference to the evaluation of surface area and pore size distribution (IUPAC Technical Report), Pure Appl. Chem. 87 (2015) 1051–1069, https://doi.org/10.1515/pac-2014-1117.

[58] B.X. Medina-Rodriguez, V. Alvarado, Use of gas adsorption and inversion methods for shale pore structure characterization, Energies 14 (2021) 2880, https://doi.org/10.3390/en14102880.

[59] D. Khan, et al., Formation and distribution of different pore types in the lacustrine calcareous shale: insights from XRD, FE-SEM, and low-pressure nitrogen adsorption analyses, ACS Omega 7 (2022) 10820–10839, https://doi.org/10.1021/acsomega.2c01001.

[60] V. Buscaglia, F. Caracciolo, C. Bottino, M. Leoni, P. Nanni, Reaction diffusion in the Y2O3-Fe2O3 system, Acta Mater. 45 (1997) 1213–1224, https://doi.org/10.1016/S1359-6454(96)00246-7.

[61] T. Norby, P. Kofstad, Proton and native-ion conductivities in Y2O3 at high temperatures, Solid State Ion. 20 (1986) 169–184, https://doi.org/10.1016/0167-2738(86)90211-0.

[62] M. Hartmanová, et al., Defect structure and physical properties of Y2O3, Solid State Ion. 36 (1989) 137–142, https://doi.org/10.1016/0167-2738(89)90157-4.

[63] U.S. Jonnalagadda, Q. Fan, X. Su, W. Liu, J.J. Kwan, Nanostructured Sonophotocatalysts for spatially controlled inertial cavitation towards energy-efficient sonochemistry, ChemCatChem 14 (2022) e202200732, https://doi.org/10.1002/cctc.202200732.